A Current Controller Design for Current Source Inverter-Fed AC Machine Drive System

Hak-Jun Lee, *Student Member, IEEE*, Sungho Jung, *Student Member, IEEE*, and Seung-Ki Sul, *Fellow, IEEE*

***Abstract*—A current source inverter (CSI) requires a capacitor filter for the commutation of switching device as well as for attenuating switching harmonics. Hence, the CSI-fed ac machine has a second-order system in the continuous time domain. This paper presents a design methodology for the closed-loop current controller of the CSI-fed ac machine drive system. A multiloop current controller design using a pole/zero cancellation method is employed with a transfer function matrix. To decouple the cross-coupling terms which cause mutual interferences between the *d*- and *q*-axes in the synchronous reference frame, two types of controller are proposed and implemented using different decoupling method. Additionally, active damping methods are incorporated to enhance the stability of the system. A stability analysis in discrete-time domain is investigated to verify the feasibility of the proposed closed-loop current controller. To evaluate the effectiveness of the proposed current controller, computer simulations and experimental tests were performed and the results are discussed.**

***Index Terms*—AC drive, current controller, current source inverter (CSI).**

I. Introduction

TRADITIONALLY, current source inverter (CSI) had been used for the high power drives due to its ruggedness to over current/short circuit and low *dv*/*dt* stress over the stator windings of the electric machine [1], [2]. Recently, because of aforementioned inherent advantages of CSI, effort has been increased to drive the ac system with CSI in high power drives such as wind power generation and hybrid electric vehicles [3]–[5].

There was a comparative study with consideration on the selection of power semiconductors for CSI [6]. In this paper, the insulated gate bipolar transistor (IGBT) is adopted to increase the switching frequency more than 1 kHz even in multi-MW drive systems because the cost and size of passive components can be reduced as the switching frequency is increased [6]. A CSI-fed electric machine can be depicted as shown in Fig. 1. A three-phase filter capacitor C_s is required for the commutation of switching devices and for filtering out the current harmonics flowing into the electric machine.

Due to this filter capacitor, the CSI-fed drive system has an inherent issue with *LC* resonance. The filter capacitor forms an *LC* filter along with the stator inductance of the electric machine and step current input from the output of the CSI can incur oscillation in the phase currents. Because a passive damping method with a physical resistor results in excessive energy losses, there were many studies to dampen the *LC* resonance with active control strategies. In order to reduce the resonance, there were several approaches which are the virtual resistor damping method [7], an active damping method using inductor current feedback control [8], a feed forward compensation method from the *LC* filter model [9], a compensator design method [10], and a hybrid-type method with a virtual resistor and a compensator [11] for the open-loop control. On the other hand, for the closed-loop control, the multiloop controller can generally be used to control the output with a higher order plant such as the CSI-fed drive system employing an *LC* filter [12]. There were studies about the multiloop controller for the voltage source inverter (VSI) with an LCL filter and CSI with an LC filter [12], [13]. In these studies, the proportional and resonant controller was used to attenuate the resonance instead of the PI controller in the synchronous reference frame.

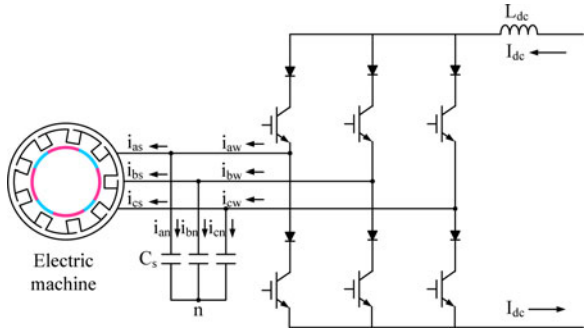

Fig. 1. Block diagram of IGBT-based CSI-fed an electric machine.

In this paper, the multiloop current controller based on two stages modeling of the CSI-fed ac machine drive system in the synchronous reference frame is proposed. As a current controller, a simple PI controller is employed and its gains are set in the technical optimum, which cancel the poles of plant by the zeros of the controller in the synchronous reference frame. With the proposed controller, the transfer function between the actual stator current and its reference can be designed as a second-order low-pass filter. The gains for the current controller can be easily determined by *LC* parameters of CSI. Two kinds of decoupling methods are addressed to compensate the coupling term which is incurred by coordinate transformation to the synchronous reference frame. In addition, active damping methods using virtual resistance are also embedded in the controller to avoid the unstable characteristics due to the parameter error and other

Manuscript received December 5, 2011; revised April 4, 2012; accepted July 3, 2012. Date of current version October 12, 2012. Recommended for publication by Associate Editor K. M. Ralph.

The authors are with the Department of Electrical Engineering and Computer Science, Seoul National University, Daehak dong, Gwanak-Gu 151-744, Korea (e-mail: hjlee@eepel.snu.ac.kr; sungho@eepel.snu.ac.kr; sulsk@plaza.snu.ac.kr).

Color versions of one or more of the figures in this paper are available online at http://ieeexplore.ieee.org.

Digital Object Identifier 10.1109/TPEL.2012.2208985

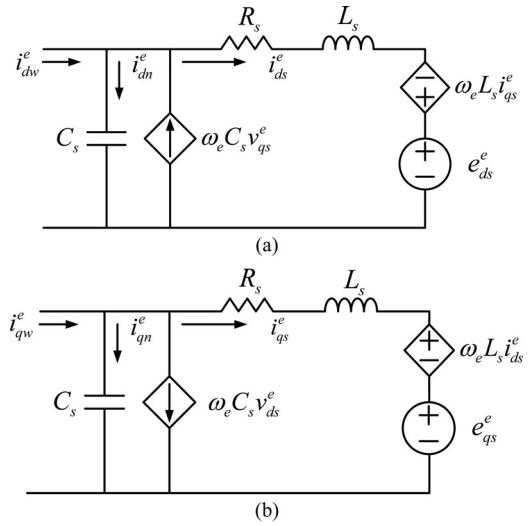

Fig. 2. Equivalent circuit of CSI including the ac system and capacitor filter in the synchronous reference frame. (a) d-axis equivalent circuit. (b) q-axis equivalent circuit.

disturbances such as digital delay. The stability analysis of the drive system with the proposed current regulator including the active damping methods is investigated in discrete-time domain. Simulation and experimental results are shown to demonstrate the effectiveness of the proposed methods.

II. System Description

The CSI-fed ac machine drive system in synchronous reference frame can be modeled as (1)–(3). The voltage and current equation of a nonsalient ac machine is employed for modeling such as an induction machine or a surface mounted permanent magnet synchronous machine (SMPMSM) or a synchronous reluctance machine

$$\begin{bmatrix} i^e_{dw} \\ i^e_{qw} \end{bmatrix} = \begin{bmatrix} i^e_{ds} \\ i^e_{qs} \end{bmatrix} + \begin{bmatrix} i^e_{dn} \\ i^e_{qn} \end{bmatrix} \tag{1}$$

$$\begin{bmatrix} i^e_{dn} \\ i^e_{qn} \end{bmatrix} = \begin{bmatrix} pC_s & -\omega_e C_s \\ \omega_e C_s & pC_s \end{bmatrix} \begin{bmatrix} v^e_{ds} \\ v^e_{qs} \end{bmatrix} \tag{2}$$

$$\begin{bmatrix} v^e_{ds} \\ v^e_{qs} \end{bmatrix} = \begin{bmatrix} R_s + pL_s & -\omega_e L_s \\ \omega_e L_s & R_s + pL_s \end{bmatrix} \begin{bmatrix} i^e_{ds} \\ i^e_{qs} \end{bmatrix} + \begin{bmatrix} e^e_{ds} \\ e^e_{qs} \end{bmatrix} \tag{3}$$

where i^e_{dqw} denotes d- and q-axes output current of a CSI, i^e_{dqs} denotes d- and q-axes stator current of an ac machine, i^e_{dqn} denotes d- and q-axes current of a filter capacitor, v^e_{dqs} denotes d- and q-axes voltage of a filter capacitor, R_s denotes a stator resistance of an ac machine, L_s denotes a synchronous inductance of an ac machine, ω_e denotes a synchronous angular speed of an ac machine, e^e_{dqs} denotes a back-emf voltage of an ac machine, and p denotes a differential operator. From those equations, the equivalent circuit can be derived as shown in Fig. 2.

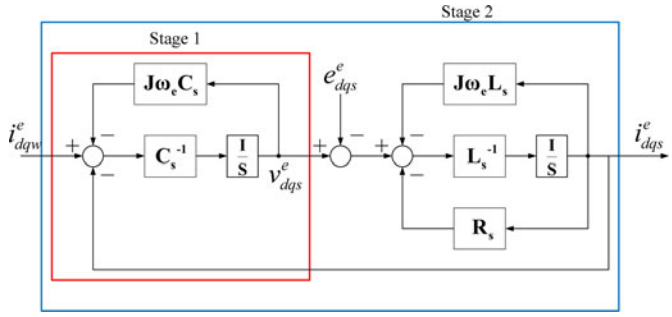

Fig. 3. Block diagram of two stage modeling.

III. Current Controller Design

The block diagram of the system model can be simply drawn as shown in Fig. 3 using the Laplace operator "s," where $\mathbf{J} = \begin{bmatrix} 0 & -1 \\ 1 & 0 \end{bmatrix}$.

The current controller can be designed based on the block diagram. In the State 1, the P controller can be employed to control the capacitor voltage v^e_{dqs} and the coupling term $\mathbf{J}\omega_e\mathbf{C}_s v^e_{dqs}$ can be decoupled by a feed forward method. In the Stage 2, the PI controller can be proposed to control stator current of an ac machine i^e_{dqs} where the coupling term can be decoupled by simple feed forwarding term or by the integrator with coupling error term which was already introduced as a complex vector current control concept [14].

A. Current Controller Design With the Feed Forward Decoupling Method

Fig. 4 shows the multiloop current control structure of an CSI-fed ac machine. In the multiloop control structure, an inner control loop which means the phase voltage control loop is designed as the P controller. The transfer function of the phase voltage control loop can be designed as the first-order low-pass filter with the P controller. Under the assumption that the synthesized current by pulsewidth modulation (PWM) is the same with the current reference on average $i^{e*}_{dqw} = i^e_{dqw}$, the output of the controller can be expressed by (4) where superscript "$*$" and K_{pv} stand for the reference and the P gain, respectively

$$\begin{aligned} \begin{bmatrix} i^{e\,*}_{dw} \\ i^{e\,*}_{qw} \end{bmatrix} &= \begin{bmatrix} K_{pv} & 0 \\ 0 & K_{pv} \end{bmatrix} \begin{bmatrix} v^{e\,*}_{ds} - v^e_{ds} \\ v^{e\,*}_{qs} - v^e_{qs} \end{bmatrix} + \begin{bmatrix} i^e_{dw\_ff} \\ i^e_{qw\_ff} \end{bmatrix} \\ &= \begin{bmatrix} i^e_{ds} \\ i^e_{qs} \end{bmatrix} + \begin{bmatrix} sC_s & -\omega_e C_s \\ \omega_e C_s & sC_s \end{bmatrix} \begin{bmatrix} v^e_{ds} \\ v^e_{qs} \end{bmatrix}. \end{aligned} \tag{4}$$

If the feed forwarding term is well matched to the real plant, then the transfer function in the first stage can be set as a first-order low-pass filter by setting K_{pv} as $C_s\omega_{c1}$. And, ω_{c1} is the cutoff frequency of the low-pass filter. Thus, closed-loop transfer function of the phase voltage control loop can be expressed by

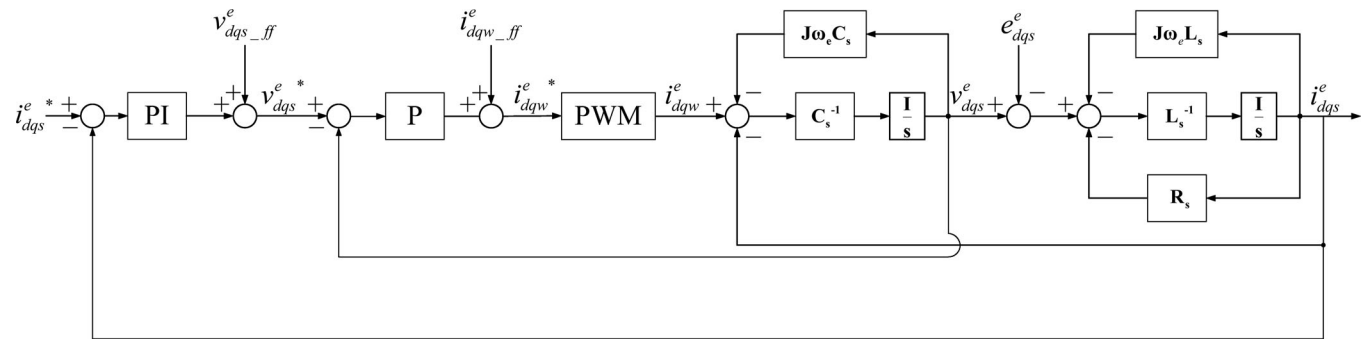

Fig. 4. Block diagram of the multiloop current controller.

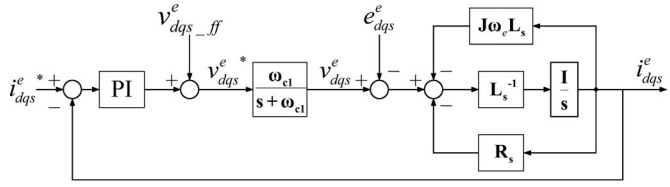

Fig. 5. Block diagram of a second stage controller design.

(5) with the feed forwarding term in (6)

$$\begin{bmatrix} v_{ds}^e \\ v_{qs}^e \end{bmatrix} = \begin{bmatrix} \dfrac{K_{pv}}{sC_s + K_{pv}} & 0 \\ 0 & \dfrac{K_{pv}}{sC_s + K_{pv}} \end{bmatrix} \begin{bmatrix} v_{ds}^{e\,*} \\ v_{qs}^{e\,*} \end{bmatrix} = \begin{bmatrix} \dfrac{\omega_{c1}}{s + \omega_{c1}} & 0 \\ 0 & \dfrac{\omega_{c1}}{s + \omega_{c1}} \end{bmatrix} \begin{bmatrix} v_{ds}^{e\,*} \\ v_{qs}^{e\,*} \end{bmatrix} \tag{5}$$

$$\begin{bmatrix} i_{dw\_ff}^e \\ i_{qw\_ff}^e \end{bmatrix} = \begin{bmatrix} i_{ds}^e \\ i_{qs}^e \end{bmatrix} + \begin{bmatrix} 0 & -\omega_e C_s \\ \omega_e C_s & 0 \end{bmatrix} \begin{bmatrix} v_{ds}^e \\ v_{qs}^e \end{bmatrix}. \tag{6}$$

In order to construct the outer control loop, the closed-loop transfer function of the inner control loop should be considered. From (5), the transfer function of the inner loop can be deduced as the first-order low-pass filter form as shown in Fig. 5. Thus, the first-order low-pass filter should be considered to decouple the coupling term $\mathbf{J}\omega_\mathbf{e}\mathbf{L_s}i_{dqs}^e$ using the feed forwarding term. The transfer function of the outer control loop, which means the phase current control loop, can be set as the second-order low pass filter if filtered feed forwarding term decouples the coupling term.

As shown in Figs. 4 and 5, the voltage reference comes from the PI controller in the multiloop control structure. The filtered voltage reference is the same with the input voltage of the ac machine, which is expressed as (5). Thus, (5) can be formulated as (7) using (3)

$$\frac{\omega_{c1}}{s + \omega_{c1}} \left(\begin{bmatrix} K_{pd} + \dfrac{K_{id}}{s} & 0 \\ 0 & K_{pq} + \dfrac{K_{iq}}{s} \end{bmatrix} \begin{bmatrix} i_{ds}^{e\,*} - i_{ds}^e \\ i_{qs}^{e\,*} - i_{qs}^e \end{bmatrix} + \begin{bmatrix} v_{ds\_ff}^e \\ v_{qs\_ff}^e \end{bmatrix} \right) = \begin{bmatrix} sL_s + R_s & -\omega_e L_s \\ \omega_e L_s & sL_s + R_s \end{bmatrix} \begin{bmatrix} i_{ds}^e \\ i_{qs}^e \end{bmatrix} + \begin{bmatrix} e_{ds}^e \\ e_{qs}^e \end{bmatrix}. \tag{7}$$

From aforementioned equation, if *P* gains ($K_{pd},\ K_{pq}$) are set as $L_s\omega_{c2},\ L_s\omega_{c2}$ respectively, and *I* gains ($K_{id},\ K_{iq}$) are set as $R_s\omega_{c2}$, then the transfer function can be deduced as (9) from (7) with the feed forwarding terms in (8)

$$\begin{bmatrix} v_{ds\_ff}^e \\ v_{qs\_ff}^e \end{bmatrix} = \frac{s + \omega_{c1}}{\omega_{c1}} \left(\begin{bmatrix} 0 & -\omega_e L_s \\ \omega_e L_s & 0 \end{bmatrix} \begin{bmatrix} i_{ds}^e \\ i_{qs}^e \end{bmatrix} + \begin{bmatrix} e_{ds}^e \\ e_{qs}^e \end{bmatrix} \right). \tag{8}$$

$$\begin{bmatrix} i_{ds}^e \\ i_{qs}^e \end{bmatrix} = \begin{bmatrix} \dfrac{\omega_{c1}\omega_{c2}}{s^2 + \omega_{c1}s + \omega_{c1}\omega_{c2}} & 0 \\ 0 & \dfrac{\omega_{c1}\omega_{c2}}{s^2 + \omega_{c1}s + \omega_{c1}\omega_{c2}} \end{bmatrix} \times \begin{bmatrix} i_{ds}^{e\,*} \\ i_{qs}^{e\,*} \end{bmatrix}. \tag{9}$$

To calculate the feed forwarding term in (8), it seems that the differentiation for the measured current is required. However, the differentiation can be circumvented as (10) with the measured voltage and current using the parameters of the ac machine

$$\begin{bmatrix} sL_s & 0 \\ 0 & sL_s \end{bmatrix} \begin{bmatrix} i_{ds}^e \\ i_{qs}^e \end{bmatrix} = \begin{bmatrix} v_{ds}^e \\ v_{qs}^e \end{bmatrix} - \begin{bmatrix} R_s & -\omega_e L_s \\ \omega_e L_s & R_s \end{bmatrix} \begin{bmatrix} i_{ds}^e \\ i_{qs}^e \end{bmatrix} - \begin{bmatrix} e_{ds}^e \\ e_{qs}^e \end{bmatrix}. \tag{10}$$

In general, the mechanical time constant is quite lager than the electric time constant. Thus, the electric angular speed can be assumed as constant in a sampling period. And also, the ac machine is usually driven with a constant *d*-axis flux in synchronous reference frame. Under the aforementioned assumptions, the back-emf can be considered as a constant value. So, the feed forwarding term for the back-emf component can be set as follows:

$$\frac{s + \omega_{c1}}{\omega_{c1}} \begin{bmatrix} e_{ds}^e \\ e_{qs}^e \end{bmatrix} = \begin{bmatrix} e_{ds}^e \\ e_{qs}^e \end{bmatrix}. \tag{11}$$

B. Decoupling Method Using Complex Current Control Concept

Instead of the feed forwarding compensation, the coupling terms can be decoupled by the integrator with coupling error term, which was already known as a complex vector current controller [14]. The design procedure for the integrator is the same with above except feed forwarding terms. The (7) can be

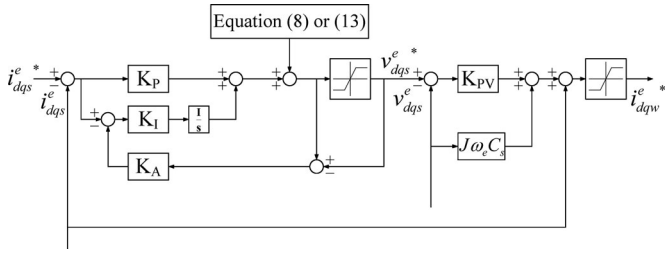

Fig. 6. Block diagram of the designed multiloop controller.

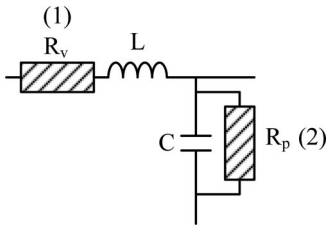

Fig. 7. Possible locations of the virtual resistor.

rewritten as the following equation to incorporate the decoupling terms:

$$\frac{\omega_{c1}}{s+\omega_{c1}}\left(\begin{bmatrix} K_{pd}+\dfrac{K_{id}}{s} & \dfrac{K_{idq}}{s} \\ \dfrac{K_{iqd}}{s} & K_{pq}+\dfrac{K_{iq}}{s}\end{bmatrix}\begin{bmatrix} i_{ds}^{e\,*}-i_{ds}^{e} \\ i_{qs}^{e\,*}-i_{qs}^{e}\end{bmatrix} + \begin{bmatrix} v_{ds\_ff}^{e} \\ v_{qs\_ff}^{e}\end{bmatrix}\right)=\begin{bmatrix} sL_s+R_s & -\omega_e L_s \\ \omega_e L_s & sL_s+R_s\end{bmatrix}\begin{bmatrix} i_{ds}^{e} \\ i_{qs}^{e}\end{bmatrix}+\begin{bmatrix} e_{ds}^{e} \\ e_{qs}^{e}\end{bmatrix}. \tag{12}$$

If the coupled integrator gains (K_{idq}, K_{iqd}) are set as $-\omega_e L_s \omega_{c2}$, $\omega_e L_s \omega_{c2}$, respectively, then the transfer function is the same with (9). The required feed forwarding terms are only back-emf component shown as follows:

$$\begin{bmatrix} v_{ds\_ff}^{e} \\ v_{qs\_ff}^{e}\end{bmatrix}=\frac{s+\omega_{c1}}{\omega_{c1}}\begin{bmatrix} e_{ds}^{e} \\ e_{qs}^{e}\end{bmatrix}=\begin{bmatrix} e_{ds}^{e} \\ e_{qs}^{e}\end{bmatrix}. \tag{13}$$

C. Active Damping Method

To avoid instability of the designed current controller due to the parameter error or other disturbances such as digital delay and nonlinearity of the inverter, it is important to embed a virtual resistor which is already known as the active damping method. In the proposed multiloop current control scheme shown in Fig. 6, there are two possible locations of the virtual resistor in the *LC* filter circuit in Fig. 7. Series connection or parallel connection of the resistor can be implemented in the designed current controller. With the virtual resistors in Fig. 7, the *d*- and *q*-axes equivalent circuits in the synchronous reference frame can be deduced as shown in Fig. 8.

As shown in Fig 9, the virtual resistor R_v which is connected to the inductor in series (series active damping method) can be easily implemented with adding the feed forwarding terms

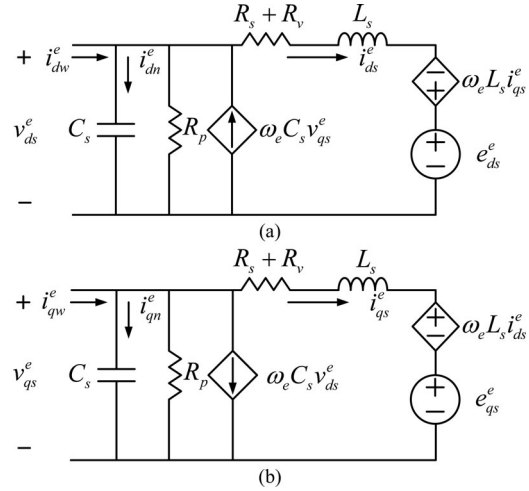

Fig. 8. Equivalent circuit of CSI including ac system and capacitor filter with virtual resistor in synchronous reference frame. (a) *d*-axis equivalent circuit. (b) *q*-axis equivalent circuit.

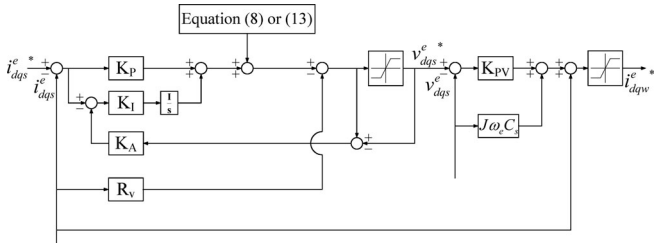

Fig. 9. Multiloop current controller with the position (1) of virtual resistor in Fig. 7 (series active damping method).

which is set as $-R_v i_{dqs}^e$, and the simple modification of the integrator gains (K_{id}, K_{iq}), which are set as$(R_s+R_v)\omega_{c2}$.

Fig. 10 shows the parallel active damping method where the virtual resistor R_p is connected to the capacitor in parallel. The additional integrator and the additional feed forwarding term are employed in the voltage control loop in order to embed the virtual resistor which is connected to the capacitor in parallel. The feed forwarding term for the parallel virtual resistor can be set as $-v_{dqs}^e/R_p$. Then, the output of the phase voltage controller can be expressed as follows:

$$\begin{bmatrix} i_{dw}^{e\,*} \\ i_{qw}^{e\,*}\end{bmatrix}=\begin{bmatrix} K_{pv}+\dfrac{K_{iv}}{s} & 0 \\ 0 & K_{pv}+\dfrac{K_{iv}}{s}\end{bmatrix}\begin{bmatrix} v_{ds}^{e\,*}-v_{ds}^{e} \\ v_{qs}^{e\,*}-v_{qs}^{e}\end{bmatrix} + \begin{bmatrix} i_{dw\_ff}^{e} \\ i_{qw\_ff}^{e}\end{bmatrix}=\begin{bmatrix} i_{ds}^{e} \\ i_{qs}^{e}\end{bmatrix}+\begin{bmatrix} sC_s+\dfrac{1}{R_p} & -\omega_e C_s \\ \omega_e C_s & sC_s+\dfrac{1}{R_p}\end{bmatrix}\begin{bmatrix} v_{ds}^{e} \\ v_{qs}^{e}\end{bmatrix}. \tag{14}$$

The integrator gain K_{iv} can be set as ω_{c1}/R_p. Thus, the closed-loop transfer function of the phase voltage control loop can be expressed by (5) with the feed forwarding term in (6).

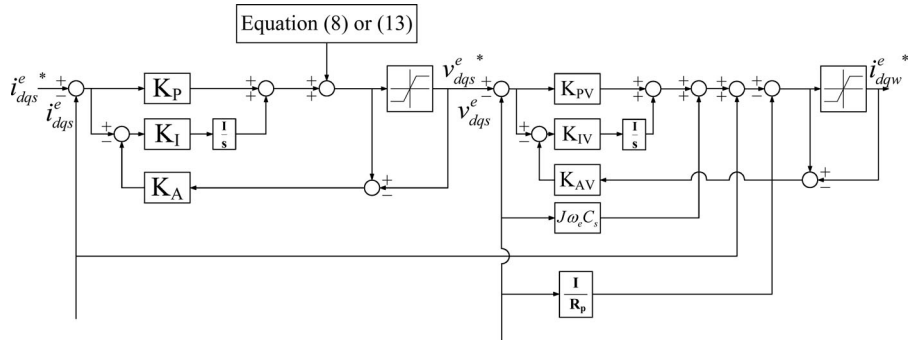

Fig. 10. Multiloop current controller with the position (2) of virtual resistor in Fig. 7 (parallel active damping method).

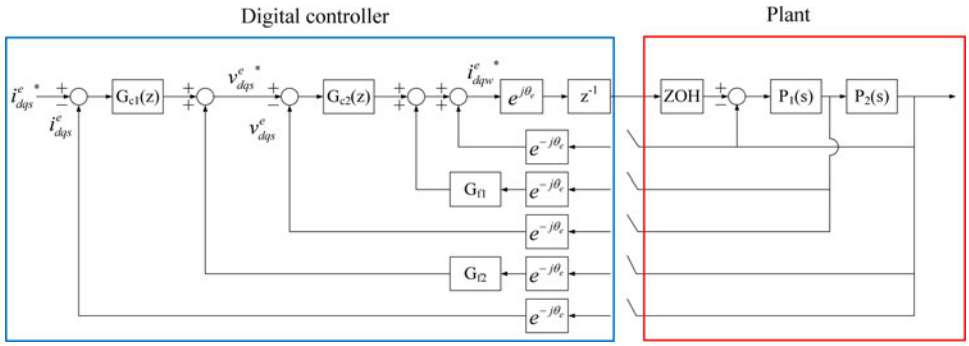

Fig. 11. Block diagram for the digital control system implementing the proposed multiloop current controller.

IV. Stability Analysis and Performance of Controller in Discrete-Time Domain

In order to analyze the stability of the proposed closed-loop control strategy, it is necessary to describe the closed loop in discrete-time domain, where the actual implementation would be done. In the case of digital control system, the zero-order hold (ZOH) equivalence is an appropriate approximation for the discrete-time domain model in sample and hold system. Thus, in most of cases, the ZOH equivalence has been commonly used for PWM input and uniformly sampled system [15]–[17].

A. Discrete-Time Model of the CSI-Fed AC Machine Drive System

If the back-emf component is decoupled by a proper feed forwarding terms, the digital control system implementing the proposed multiloop current controller is depicted Fig. 11 using a sampler and the ZOH.

In Fig. 11, $e^{j\theta_e}$ and $e^{-j\theta_e}$ stand for the reference frame transformation to the stationary reference frame and to the synchronous reference frame in complex vector, respectively. Also, z^{-1} means the unit delay which is the intrinsic time delay of the digital control system between instants of the sampling of signals and the voltage commands for PWM inputs. In the proposed multiloop controller, $G_{c2}(z)$ represents the voltage controller, and $G_{c1}(z)$ represents the current controller. In addition, G_{f1} and G_{f2} stand for the state feedback gains which can be used for the feed forwarding decoupling terms and active damping terms.

The transfer matrix of the ac machine model $P_2(s)$ can be expressed using inductance and resistance as expressed in the following equation, because of decoupling of back-emf of the ac machine:

$$P_2(s) = \begin{bmatrix} R_s + sL_s & 0 \\ 0 & R_s + sL_s \end{bmatrix}^{-1}. \tag{15}$$

And also, the transfer matrix of the filter capacitor can be expressed as follows:

$$P_1(s) = \begin{bmatrix} sC_s & 0 \\ 0 & sC_s \end{bmatrix}^{-1}. \tag{16}$$

When it comes to the analysis in the discrete-time domain, it should be taken into account that the z-transform of a product of cascaded transfer function is not equal to the product of z-transforms of each transfer function, shown in (17). In (17), $A(s)$ and $B(s)$are arbitrary functions for a cascaded system, and Z stands for an operator of z-transform [18]

$$Z\{A(s)B(s)\} = Z\{AB(s)\} \neq Z\{A(s)\}Z\{B(s)\}. \tag{17}$$

From (17), it can be noted that the design approach of multiloop controller based on the continuous time domain has critical defect in implementation in the discrete time domain, caused by difference between the continuous model and the discrete model. Due to this difference, the designed controller might have instability or poor performance which is not desired. In the case of the proposed multiloop current controller, the decoupling method cannot be achieved due to the property of the z-transform shown in (17) because the proposed design approach is based on

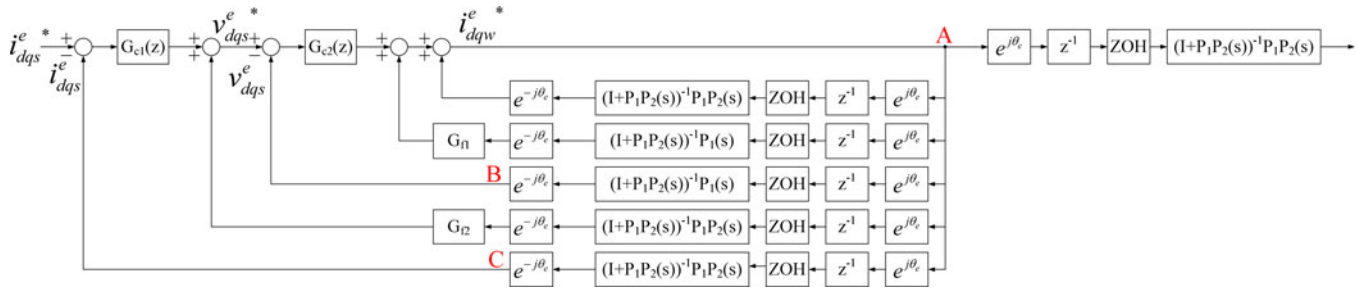

Fig. 12. Reconstructed block diagram for the digital control system.

the pole zero cancellation method in continuous time domain. Thus, the designed transfer function, which is the second-order low-pass filter in (9), might not be feasible in the digital control system. Hence, the proposed multiloop current controller should be analyzed based on the discrete-time domain.

Fig. 11 can be reconstructed as Fig. 12 with the consideration of (17).

As shown in Fig. 12, two combined transfer matrices, $(I + P_1P_2(s))^{-1}P_1(s)$ and $(I + P_1P_2(s))^{-1}P_1P_2(s)$, should be discretized in order to consider (17). Two combined transfer matrices can be expressed as (18) and (19), because the transfer matrix for the symmetric machine like SMPMSM or an induction machine can be simplified into the transfer function using complex vector variables [14], [16], [19]

$$\frac{v^s_{dqs}(s)}{{i^s_{dqw}}^*(s)} = \frac{P_1(s)}{1+P_1P_2(s)} = \frac{(sL_s+R_s)}{sC_s(sL_s+R_s)+1} = \frac{1}{(B-A)L_sC_s} \times \left(\frac{R_s-AL_s}{A}\frac{A}{(s+A)} - \frac{R_s-BL_s}{B}\frac{B}{(s+B)}\right) \tag{18}$$

$$\frac{i^s_{dqs}(s)}{{i^s_{dqw}}^*(s)} = \frac{P_1P_2(s)}{1+P_1P_2(s)} = \frac{1}{sC_s(sL_s+R_s)+1} = \frac{1}{(B-A)L_sC_s}\left(\frac{A}{(s+A)} - \frac{B}{(s+B)}\right) \tag{19}$$

where $A = \frac{(R_s/L_s)+\sqrt{(R_s^2/L_s^2)-(4/L_sC_s)}}{2}$, $B = \frac{(R_s/L_s)-\sqrt{(R_s^2/L_s^2)-(4/L_sC_s)}}{2}$, and the complex vector variables are defined as $f^s_{dq} = f^s_d + j \cdot f^s_q$.

The ZOH equivalent of (18) and (19) can deduce as given in the following equation, including the digital delay:

$$\frac{v^s_{dqs}(z)}{{i^s_{dqw}}^*(z)} = T^s_2(z) = z^{-1}\cdot(1-z^{-1}) \cdot \mathrm{Z}\left\{\frac{1}{(B-A)L_sC_s}\left(\frac{R_s-AL_s}{A}\frac{A}{s(s+A)} - \frac{R_s-BL_s}{B}\frac{B}{s(s+B)}\right)\right\}$$

$$= \frac{1}{(B-A)L_sC_s}\left(\frac{R_s-AL_s}{A}\cdot\frac{(1-e^{-AT})}{z(z-e^{-AT})} - \frac{R_s-BL_s}{B}\cdot\frac{(1-e^{-BT})}{z(z-e^{-BT})}\right) \tag{20}$$

$$\frac{i^s_{dqs}(z)}{{i^s_{dqw}}^*(z)} = T^s_1(z) = z^{-1}\cdot(1-z^{-1}) \cdot \mathrm{Z}\left\{\frac{1}{(B-A)L_sC_s}\left(\frac{A}{As(s+A)} - \frac{B}{Bs(s+B)}\right)\right\}$$

$$= \frac{1}{(B-A)L_sC_s}\left(\frac{1}{A}\cdot\frac{(1-e^{-AT})}{z(z-e^{-AT})} - \frac{1}{B}\cdot\frac{(1-e^{-BT})}{z(z-e^{-BT})}\right). \tag{21}$$

In order to construct the discrete model in a synchronous reference frame, the point A to B and A to C is considered in Fig. 12. The discrete model in the synchronous reference frame can be expressed as follows:

$$T^e_2(z) = \frac{v^e_{dqs}(z)}{{i^e_{dqw}}^*(z)} = e^{j\theta_e(z)}T^s_2(z)e^{-j\theta_e(z)} \tag{22}$$

$$T^e_1(z) = \frac{i^e_{dqs}(z)}{{i^e_{dqw}}^*(z)} = e^{j\theta_e(z)}T^s_1(z)e^{-j\theta_e(z)}. \tag{23}$$

Superscripts "*s*" and "*e*" denote stationary and synchronous reference frames in (22) and (23), respectively. In aforementioned equations, $e^{j\theta_e(z)}T^s_2(z)e^{-j\theta_e(z)}$ and $e^{j\theta_e(z)}T^s_1(z)e^{-j\theta_e(z)}$ mean the discrete-time model of the ac machine in the synchronous reference frame.

On the other hands, the synchronous angle can be expressed as (24) in the discrete-time domain. And, the reference frame transformation from the stationary reference frame to the synchronous reference frame can be defined as (25)

$$\theta_e[k+1] = \theta_e[k] + \omega_eT_s \tag{24}$$

$$f^s_{dq}[k]e^{-j\theta_e[k]} = f^e_{dq}[k] \tag{25}$$

where T_s represents a sampling period.

Thus, the equations for the reference frame transformation can be deduced in the discrete-time domain as shown in the

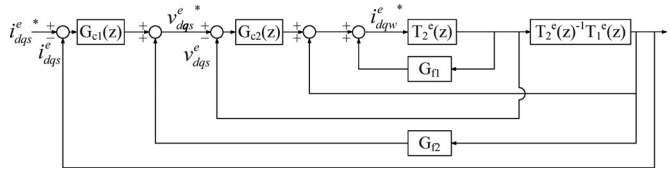

Fig. 13. Block diagram of the control system in discrete-time domain.

following equation:

$$f^s_{dq}[k+m]e^{-j\theta_e[k]} = f^s_{dq}[k+m]e^{-j\theta_e[k+m]}e^{jm\omega_e T} = f^e_{dq}[k+m]e^{jm\omega_e T} \quad (26)$$

$$z^m f^s_{dq}(z)e^{-j\theta_e(z)} = z^m\left(f^s_{dq}(z)e^{-j\theta_e(z)}\right)e^{jm\omega_e T} = z^m f^e_{dq}(z)e^{jm\omega_e T}. \quad (27)$$

If it is assumed that the general transfer function in the stationary reference frame is expressed as (28), then the transfer function in the synchronous reference frame can be expressed as (30) in the discrete time domain using (27)

$$\frac{y^s_{dq}(z)}{x^s_{dq}(z)} = \frac{\sum_{k=0}^{M} b_k z^k}{\sum_{k=0}^{N} a_k z^k} \Leftrightarrow \frac{y^s_{dq}(z)e^{-j\theta_e(z)}}{x^s_{dq}(z)e^{-j\theta_e(z)}} = \frac{\sum_{k=0}^{M} b_k z^k e^{-j\theta_e(z)}}{\sum_{k=0}^{N} a_k z^k e^{-j\theta_e(z)}} \quad (28)$$

$$\sum_{k=0}^{N} a_k z^k y^s_{dq}(z)e^{-j\theta(z)} = \sum_{k=0}^{M} b_k z^k x^s_{dq}(z)e^{-j\theta(z)}$$

$$\Leftrightarrow \sum_{k=0}^{N} a_k z^k y^e_{dq}(z)e^{jk\omega_e T} = \sum_{k=0}^{M} b_k z^k x^e_{dq}(z)e^{jk\omega_e T} \quad (29)$$

$$\frac{y^e_{dq}(z)}{x^e_{dq}(z)} = \frac{\sum_{k=0}^{M} b_k z^k e^{jk\omega_e T}}{\sum_{k=0}^{N} a_k z^k e^{jk\omega_e T}}. \quad (30)$$

From the result of (30), the discrete model in the synchronous reference frame can be expressed as follows:

$$T_1^e(z) = \frac{1}{(B-A)L_sC_s}\left(\frac{1}{A}\cdot\frac{(1-e^{-AT})}{ze^{j\omega_e T}(ze^{j\omega_e T}-e^{-AT})} - \frac{1}{B}\cdot\frac{(1-e^{-BT})}{ze^{j\omega_e T}(ze^{j\omega_e T}-e^{-BT})}\right) \quad (31)$$

$$T_2^e(z) = \frac{1}{(B-A)L_sC_s}\left(\frac{R_s-AL_s}{A}\cdot\frac{(1-e^{-AT})}{ze^{j\omega_e T}(ze^{j\omega_e T}-e^{-AT})} - \frac{R_s-BL_s}{B}\cdot\frac{(1-e^{-BT})}{ze^{j\omega_e T}(ze^{j\omega_e T}-e^{-BT})}\right). \quad (32)$$

Through aforementioned process, the block diagram for the digital control system can be finalized as given in Fig. 13.

As shown in Fig. 13, the closed-loop transfer function of the current controller in the discrete-time domain can be deduced as follows:

$$\frac{i^e_{dqs}(z)}{i^e_{dqs}{}^*(z)} = \times\frac{G_{c1}(z)G_{c2}(z)T_1^e(z)}{1-T_1^e(z)-G_{f1}T_2^e(z)-G_{f2}G_{c2}(z)T_1^e(z)+G_{c1}(z)G_{c2}(z)T_1^e(z)}. \quad (33)$$

This closed-loop transfer function is used for analyzing the performance or stability of the proposed control method. In the simulations and experiments, the electric angle delay $e^{j\omega_e T_s}$ due to the angle changes during the sampling period is compensated [16], [20]. So, in this paper, the delay compensated models which are expressed as follows are used for analyzing stability of the proposed control scheme:

$$T_1^e(z) = \frac{1}{(B-A)L_sC_s}\left(\frac{1}{A}\cdot\frac{(1-e^{-AT})}{z(ze^{j\omega_e T}-e^{-AT})} - \frac{1}{B}\cdot\frac{(1-e^{-BT})}{z(ze^{j\omega_e T}-e^{-BT})}\right) \quad (34)$$

$$T_2^e(z) = \frac{1}{(B-A)L_sC_s}\left(\frac{R_s-AL_s}{A}\cdot\frac{(1-e^{-AT})}{z(ze^{j\omega_e T}-e^{-AT})} - \frac{R_s-BL_s}{B}\cdot\frac{(1-e^{-BT})}{z(ze^{j\omega_e T}-e^{-BT})}\right). \quad (35)$$

B. Current Controller With the Feed Forward Decoupling Method

As aforementioned in Section III-A, the controllers $G_{c1}(z)$, $G_{c2}(z)$ and state feedback gains (G_{f1}, G_{f2}) can be applied to (33) as follows:

$$G_{f1} = j\omega_e C_s,\ G_{f2} = j\omega_e L_s\left(1+\frac{1-z^{-1}}{\omega_{c1}T_s}\right) \quad (36)$$

$$G_{c1}(z) = \frac{R_s}{1-z^{-1}}\omega_{c2}T_s + L_s\omega_{c2},\ G_{c2}(z) = C_s\omega_{c1}. \quad (37)$$

To analyze the stability, the migration of poles and zeroes which means the eigenvalue migration with a varying natural frequency is plotted in Fig. 14 where the designed transfer function is expressed as follows:

$$\frac{i^e_{dqs}(s)}{i^e_{dqs}{}^*(s)} = \frac{\omega_{c1}\omega_{c2}}{s^2+\omega_{c1}s+\omega_{c1}\omega_{c2}} = \frac{\omega_n^2}{s^2+2\omega_n s+\omega_n^2} \quad (38)$$

where ω_n stands for the natural frequency.

As shown in Fig. 14, all of closed-loop poles are inside of the unit circle. Thus, it can be noted that the digital control system with the feed forward decoupling method remains stable at overall the natural frequencies under consideration. Although the closed-loop poles are still inside of unit circle for the range of applied natural frequencies, the system reveals poor performances. As the natural frequency decreases, the damping ratio of the digital control system decreases (point F to E). So, the system does not have the designed damping ratio. In addition, as the natural frequency increases, the damping ratio of the digital control system also increases (point E to F). However, the two

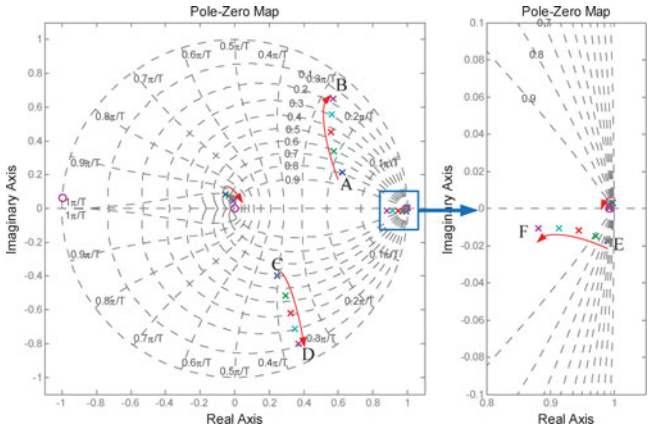

Fig. 14. Migration of poles/zeros of the digital control system according to the increase of the natural frequency (100 Hz → 500 Hz) with the feed forward decoupling method ($\omega_e = 200\pi$ rad/s, $T_s = 100\,\mu$s, $L_s = 0.7$ mH, $R_s = 50\,\text{m}\Omega$, $C_s = 75\,\mu$F).

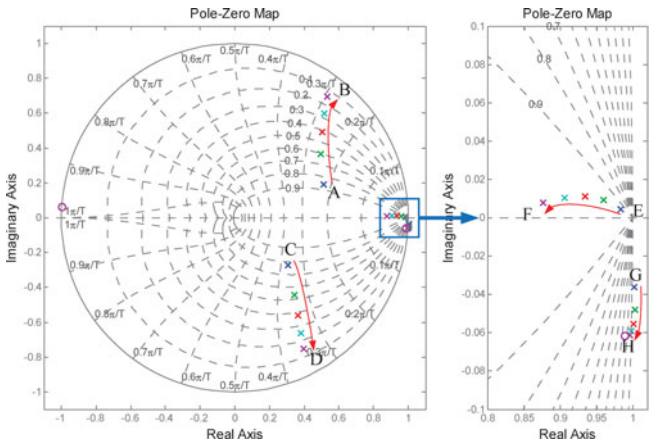

Fig. 15. Migration of poles/zeros of the digital control system according to the increase of the natural frequency (100 Hz → 500 Hz) with the complex vector decoupling method ($\omega_e = 200\pi$ rad/s, $T_s = 100\,\mu$s, $L_s = 0.7$ mH, $R_s = 50\,\text{m}\Omega$, $C_s = 75\,\mu$F).

dominant poles approach the boundary of the unit circle which results in the unstable system or highly oscillating system (point A to B, C to D).

C. Complex Vector Decoupling Method

As aforementioned in Section III-B, the controllers $G_{c1}(z)$, $G_{c2}(z)$ and the state feedback gains G_{f1}, G_{f2} can be applied to (33) as follows:

$$G_{f1} = j\omega_e C_s, \quad G_{f2} = 0 \tag{39}$$

$$G_{c1}(z) = \frac{R_s + j\omega_e L_s}{1 - z^{-1}}\omega_{c2}T_s + L_s\omega_{c2}, \quad G_{c2}(z) = C_s\omega_{c1}. \tag{40}$$

The migration of poles and zeroes with a varying natural frequency is plotted in Fig. 15.

As shown in Fig. 15, the specific poles are outside of the unit circle at the certain natural frequency (points near *G*). Thus, it can be noted that the digital control system with the complex vector decoupling method may become unstable system at specific natural frequencies under consideration. As the natural frequency increases, the system can be stable (point G to H). However, the two dominant poles approach the boundary of the unit circle which results in the unstable system or highly oscillating system (point A to B, C to D).

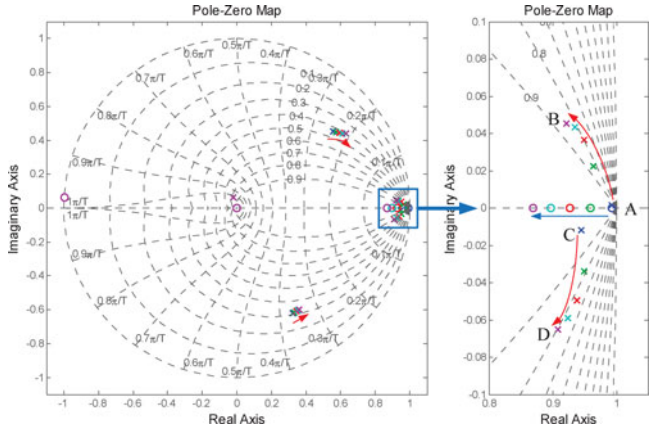

Fig. 16. Migration of poles/zeros of the digital control system according to the increase of the series virtual resistance (0 Ω → 1 Ω) with the feed forward decoupling method ($\omega_e = 200\pi$ rad/s, $\omega_n = 600\pi$ rad/s, $T_s = 100\,\mu$s, $L_s = 0.7$ mH, $R_s = 50\,\text{m}\Omega$, $C_s = 75\,\mu$F).

D. Series Active Damping Method

As aforementioned in Section III-C, there are two possible locations for embedding virtual resistors. In the case of the series active damping method with the feed forward decoupling method, the controllers $G_{c1}(z)$, $G_{c2}(z)$ and state feedback gains G_{f1}, G_{f2} can be applied to (33) as follows:

$$G_{f1} = j\omega_e C_s, \quad G_{f2} = j\omega_e L_s\left(1 + \frac{1 - z^{-1}}{\omega_{c1}T_s}\right) - R_v \tag{41}$$

$$G_{c1}(z) = \frac{R_s + R_v}{1 - z^{-1}}\omega_{c2}T_s + L_s\omega_{c2}, \quad G_{c2}(z) = C_s\omega_{c1}. \tag{42}$$

The migration of poles and zeroes according to the variation of the virtual damping resistance with the feed forward decoupling method is plotted in Fig. 16.

Fig. 16 shows that the poles adjacent to the boundary of the unit circle migrate toward inside of the unit circle as the series virtual resistance increases (point A to B, point C to D). In addition, the damping ratio increases as the virtual resistance increase.

In the case of the series active damping method for the complex vector decoupling method, the controllers $G_{c1}(z)$, $G_{c2}(z)$ and state feedback gains G_{f1}, G_{f2} can be applied to (33) as follows:

$$G_{f1} = j\omega_e C_s, \quad G_{f2} = -R_v \tag{43}$$

$$G_{c1}(z) = \frac{R_s + R_v + j\omega_e L_s}{1 - z^{-1}}\omega_{c2}T_s + L_s\omega_{c2}, \quad G_{c2}(z) = C_s\omega_{c1}. \tag{44}$$

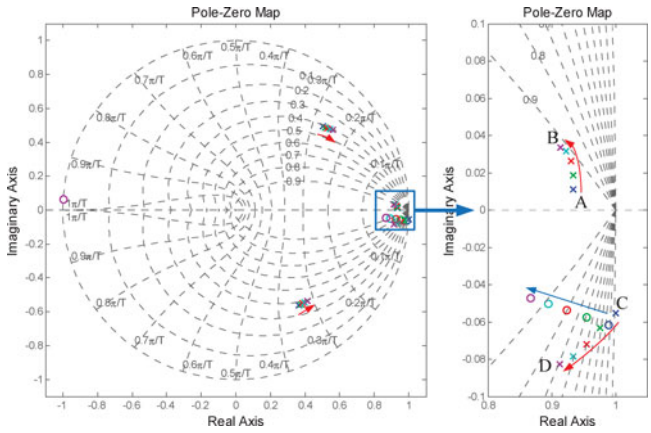

Fig. 17. Migration of poles/zeros of the digital control system according to the increase of the virtual resistance ($0\,\Omega \rightarrow 1\,\Omega$) with the complex vector decoupling method ($\omega_e = 200\pi$ rad/s, $\omega_n = 600\pi$ rad/s, $T_s = 100\,\mu$s, $L_s = 0.7$ mH, $R_s = 50$ mΩ, $C_s = 75\,\mu$F).

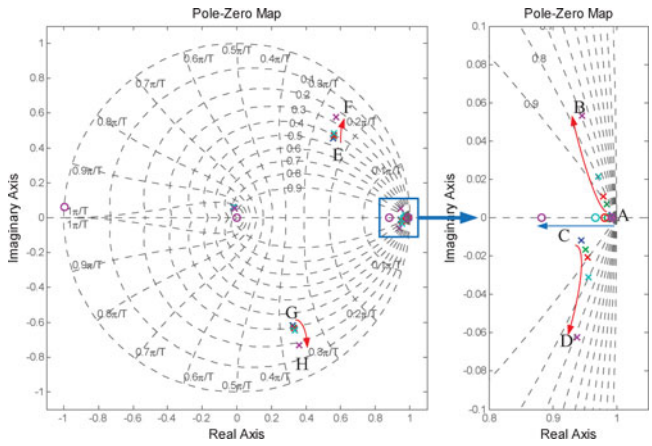

Fig. 18. Migration of poles/zeros of the digital control system according to the increase of the parallel virtual conductance ($0\,\mathrm{S} \rightarrow 0.1\,\mathrm{S}$) with the feed forward decoupling method ($\omega_e = 200\pi$ rad/s, $\omega_n = 600\pi$ rad/s, $T_s = 100\,\mu$s, $L_s = 0.7$ mH, $R_s = 50$ mΩ, $C_s = 75\,\mu$F).

The migration of poles and zeroes according to the variation of the virtual damping resistance for the complex decoupling method is plotted in Fig. 17.

As shown in Fig. 17, the pole outside of the unit circle migrates to the inside of unit circle (point C to D). Thus, the unstable system is changed to the stable system as the series virtual resistance increases. It can be noted that the complex vector decoupling method with the series active damping method has almost same characteristics to those of the feed forward decoupling method with the series active damping method which is shown in Fig. 16.

E. Parallel Active Damping Method

In the case of the parallel active damping method for the feed forward decoupling method, the controllers $G_{c1}(z), G_{c2}(z)$ and state feedback gains G_{f1}, G_{f2} can be applied to (33) as follows:

$$G_{f1} = j\omega_e C_s - g_p, \quad G_{f2} = j\omega_e L_s \left(1 + \frac{1 - z^{-1}}{\omega_{c1} T_s}\right) \tag{45}$$

$$G_{c1}(z) = \frac{R_s}{1 - z^{-1}}\omega_{c2} T_s + L_s \omega_{c2}$$

$$G_{c2}(z) = \frac{g_p}{1 - z^{-1}}\omega_{c1} T_s + C_s \omega_{c1}. \tag{46}$$

where g_p stands for an conductance of the parallel virtual resistor $g_p = 1/R_p$.

The migration of poles and zeroes according to the variation of the parallel virtual resistance for the feed forward decoupling method is plotted in Fig. 18.

Fig. 18 shows that the poles approach the boundary of the unit circle (point E to F, point G to H) and the damping ratio of the system increases (point A to B, point C to D) as the virtual conductance increases. Thus, the system might have highly oscillatory response or poor dynamic response.

On the other hand, in the case of the parallel active damping method for the complex vector decoupling method, the controllers $G_{c1}(z), G_{c2}(z)$ and state feedback gains G_{f1}, G_{f2} can

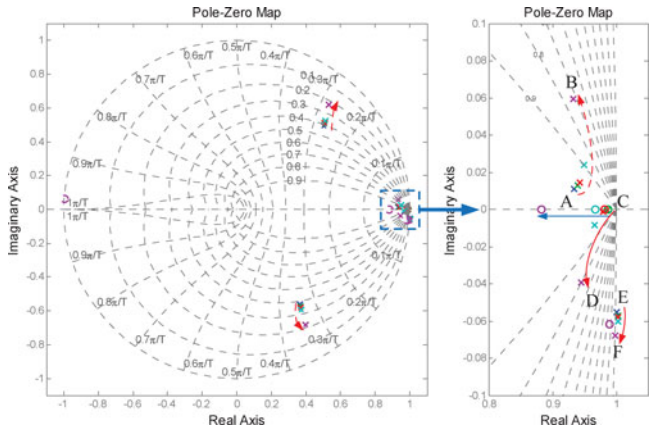

Fig. 19. Migration of poles/zeros of the digital control system according to the increase of the parallel virtual conductance ($0\,\mathrm{S} \rightarrow 0.1\,\mathrm{S}$) with the complex vector decoupling method ($\omega_e = 200\pi$ rad/s, $\omega_n = 600\pi$ rad/s, $T_s = 100\,\mu$s, $L_s = 0.7$ mH, $R_s = 50$ mΩ, $C_s = 75\,\mu$F).

be applied to (33) as follows:

$$G_{f1} = j\omega_e C_s - g_p, \quad G_{f2} = 0 \tag{47}$$

$$G_{c1}(z) = \frac{R_s + j\omega_e L_s}{1 - z^{-1}}\omega_{c2} T_s + L_s \omega_{c2}$$

$$G_{c2}(z) = \frac{g_p}{1 - z^{-1}}\omega_{c1} T_s + C_s \omega_{c1}. \tag{48}$$

The migration of poles and zeroes according to the variation of the parallel virtual resistor for the feed forward decoupling method is plotted in Fig. 19.

As shown in Fig. 19, some poles are still out of the unit circle although the parallel virtual conductance increases (point E to F). It can be noted that the system might remain unstable in spite of increased damping gain. Additionally, other poles approach the boundary of the unit circle and the damping ratio decreases (point A to B, point C to D) if the damping gain (parallel virtual conductance) increases enough so that the system is stable. Thus, the parallel virtual resistor might not guarantee the improved stability and dynamic responses.

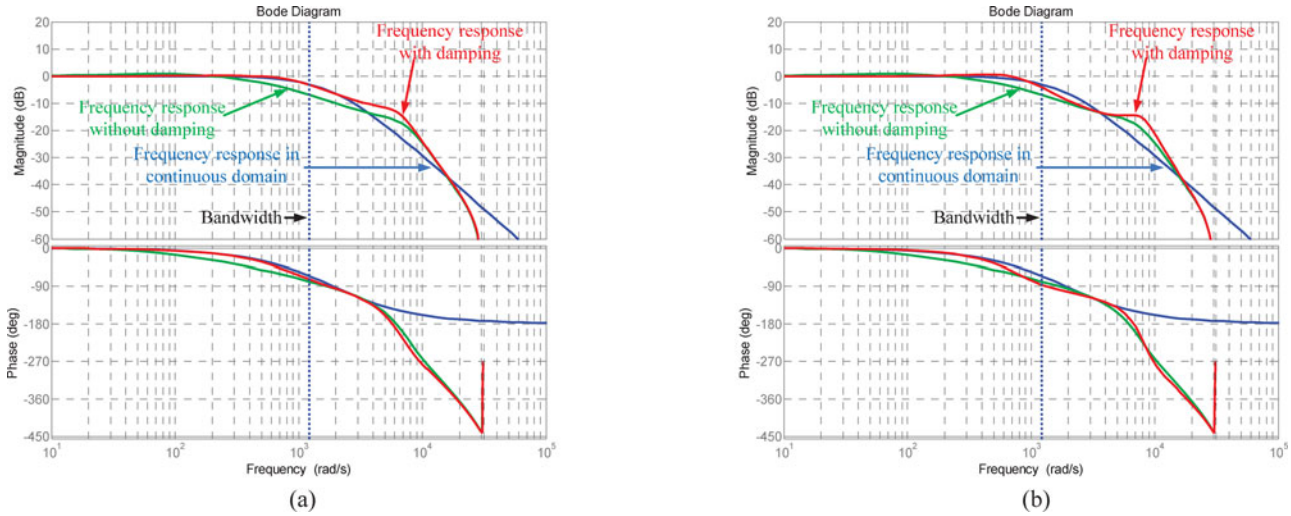

Fig. 20. Bode plot of the digital control system for the feed forward decoupling method ($\omega_e = 200\pi$ rad/s, $\omega_n = 600\pi$ rad/s, $T_s = 100\,\mu$s, $L_s = 0.7$ mH, $R_s = 50\,\mathrm{m}\Omega$, $C_s = 75\,\mu$F). (a) With the series active damping method. (b) With the parallel active damping method.

From the aforementioned analysis, it can be concluded that the parallel active damping method is not effective to improve the control performance of the proposed two kinds of control structures than the series active damping method is.

F. Command Tracking Bandwidth of the Designed Controller

The designed transfer function of the system can be expressed as (49) which is mentioned in Section III. And also, it can be expressed as the general second-order low-pass filter form with a damping ratio, ζ, and a natural frequency ω_n

$$\frac{i^e_{dqs}(s)}{{i^e_{dqs}}^*(s)} = \frac{\omega_{c1}\omega_{c2}}{s^2 + \omega_{c1}s + \omega_{c1}\omega_{c2}} = \frac{\omega_n^2}{s^2 + 2\zeta\omega_n s + \omega_n^2}. \quad (49)$$

In general, the bandwidth of the transfer function can be defined as the cutoff frequency where has attenuated gain of 3 dB with respect to the dc gain. In the case of the second-order low-pass filter, the bandwidth depends on the damping ratio and the natural frequency.

In this paper, the damping ratio of 1 was used for the fastest response without overshoot (critically damped responses). Thus, the bandwidth of the system can be deduced as (50). And, the natural frequency is equal to the system poles location

$$\omega_{\mathrm{BW}} = \omega_n\sqrt{\sqrt{2} - 1} \approx 0.6436\omega_n \quad (50)$$

where ω_{BW} stands for the bandwidth.

On the other hands, a settling time can be a significant concern to determine the bandwidth of the system in the step response. In the critically damped system, the settling time can be expressed as follows:

$$e^{-\omega_n t_{st}}(1 + \omega_n t_{st}) = 0.02 \quad (51)$$

where t_{st} stands for the settling time.

It can be noted that the proper choice of the natural frequency is important to satisfy the dynamics of the general applications. In many applications, such as a traction motor drive, a hybrid vehicle system and a wind turbine generation system, the step response might be considered significantly. Thus, the natural frequency should be chosen for the reasonable settling time.

The designed controller based on the continuous system might not have the desired bandwidth because of the difference between the continuous model and the discrete model of the cascaded system. The Bode plot of the proposed controller for the frequency responses with two active damping methods is depicted in Figs. 20 and 21.

As shown in Figs. 20 and 21, the frequency responses in the discrete-time domain are different from the frequency responses in continuous time domain. Thus, the transfer function in the discrete-time domain does not meet the desired bandwidth which is designed in the continuous time domain. The parallel active damping method is not effective to compensate the different bandwidth. However, with the series active damping method, the control system can achieve the desired bandwidth effectively.

G. Parametric Error Dependence

As mentioned earlier, the parallel active damping method is not effective to improve the control performance than the series active damping method. So, an analysis with the series active damping method is quite reasonable approach for the parametric error dependence.

Figs. 22 and 23 show the migration of poles and zeroes with the variation of the series virtual resistance for the two decoupling method. And, it is assumed that the estimated parameters for setting the controller's gains have errors in the inductance and resistance, $\hat{L}_s = 1.5 \times L_s$, $\hat{R}_s = 0.5 \times R_s$, $\hat{C}_s = C_s$, where $\hat{L}_s$, $\hat{R}_s$ and $\hat{C}_s$ stand for the estimated inductance, resistance, and capacitance, respectively.

Fig. 22 shows that the poles adjacent to the boundary of the unit circle migrate toward inside of the unit circle as the series virtual resistance increases (point A to B) regardless of the parametric errors. In addition, the dominant poles do not change significantly.

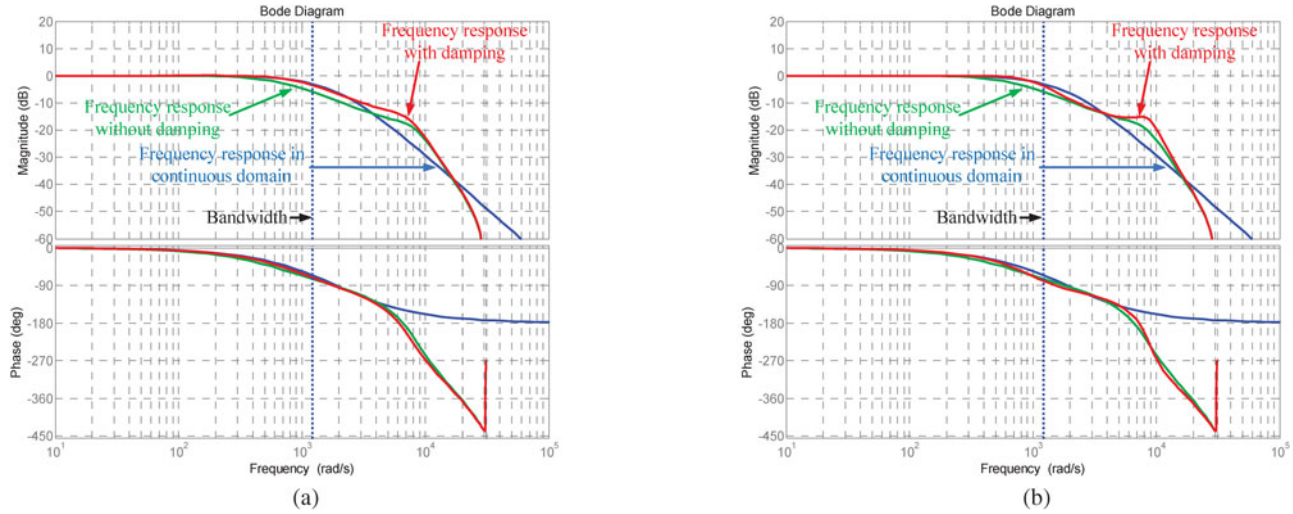

Fig. 21. Bode plot of the digital control system for the complex vector decoupling method ($\omega_e = 200\pi$ rad/s, $\omega_n = 600\pi$ rad/s, $T_s = 100\,\mu$s, $L_s = 0.7$ mH, $R_s = 50\,\mathrm{m}\Omega$, $C_s = 75\,\mu$F). (a) With the series active damping method. (b) With the parallel active damping method.

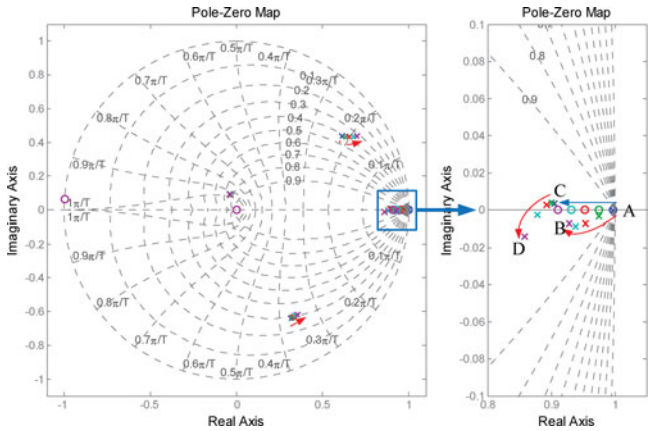

Fig. 22. Migration of poles/zeros of the digital control system according to the increase of the series virtual resistance ($0\,\Omega \rightarrow 1\,\Omega$) with the parametric error in inductance and resistance for the feed forward decoupling method ($\omega_e = 200\pi$ rad/s, $T_s = 100\ \mu$s, $\hat{L}_s = 1.5 \times L_s$, $\hat{R}_s = 0.5 \times R_s$, $\hat{C}_s = C_s$).

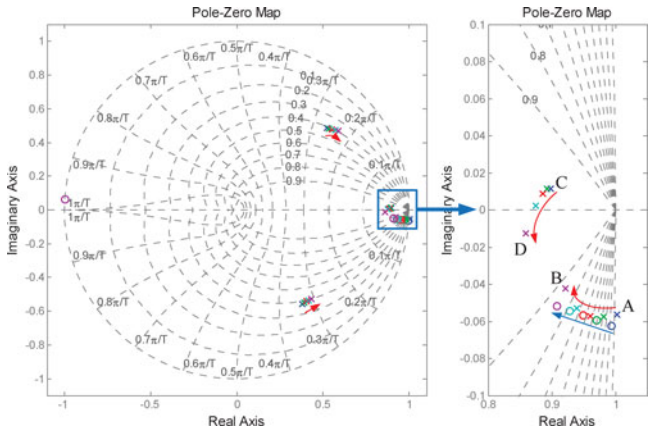

Fig. 23. Migration of poles/zeros of the digital control system according to the increase of the series virtual resistance ($0\,\Omega \rightarrow 1\,\Omega$) with the parametric error in inductance and resistance for the complex vector decoupling method ($\omega_e = 200\pi$ rad/s, $T_s = 100\ \mu$s, $\hat{L}_s = 1.5 \times L_s$, $\hat{R}_s = 0.5 \times R_s$, $\hat{C}_s = C_s$).

As shown in Fig. 23, the pole lies at the outside of the unit circle migrates to the inside of the unit circle (point A to B) as the series virtual resistance increases regardless of the parametric errors. Thus, the unstable system is changed to the stable system. And also, the dominant poles are changed slightly.

However, the estimated capacitance is related to the pole of the inner control loop which is the phase voltage control loop, and the parametric error cannot be compensated using the damping method. So, the proposed multiloop current control is sensitive to the parametric error in the capacitance. Fig. 24 shows the migration of poles and zeroes according to the parameter error of the capacitance from $\hat{C}_s = C_s$ to $\hat{C}_s = 2 \times C_s$ for the two decoupling method with the series virtual resistance 1 Ω. And, it is assumed that the other estimated parameters have also error like $\hat{L}_s = 1.5 \times L_s$, $\hat{R}_s = 0.5 \times R_s$.

As shown in Fig. 24, the two dominant poles approach to and finally go out of the boundary of the unit circle as the capacitance error increases, which results in the unstable system (point A to B, C to D).

From aforementioned results, it can be noted that the two decoupling methods with the series active damping method are robust to the parametric error in the inductance and resistance, but not to the parametric error in the capacitance.

V. Simulation Results

To evaluate the performance of the proposed multiloop current controller, the computer simulation for SMPMSM has been done using PSIM software. The parameters for simulation are listed in Table I.

In the simulation, the electric angular speed of the rotor is set to 200π rad/s and the dc-link current, as 40-A constant. In addition, the transfer function from the reference current to the real current is designed as follows:

$$\frac{\omega_n^2}{s^2 + 2\omega_n s + \omega_n^2},\ \omega_n = 600\pi\,[\mathrm{rad/s}]. \tag{52}$$

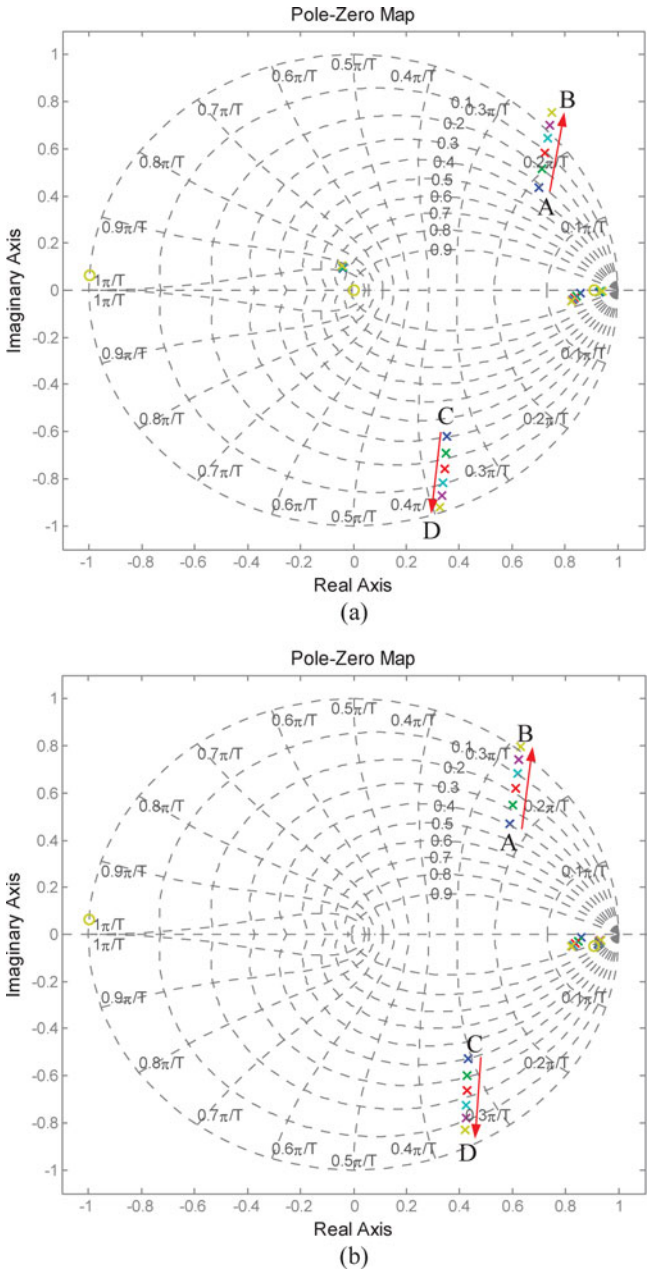

Fig. 24. Migration of poles/zeros of the digital control system according to the variation of the error in the estimated capacitance ($\hat{C}_s = C_s \rightarrow \hat{C}_s = 2 \times C_s$) and the parametric error in inductance and resistance ($\omega_e = 200\pi$ rad/s, $T_s = 100\ \mu$s, $\hat{L}_s = 1.5 \times L_s$, $\hat{R}_s = 0.5 \times R_s$, $R_v = 1\ \Omega$).

TABLE I
PARAMETERS OF SMPMSM

Parameter	Values
Rated Power	11 kW
Rated Speed	1500 r/min
Number of Poles	8
Back EMF constant	0.1478 V/(rad/s)
Synchronous d axis inductance	0.7 mH
Synchronous q axis inductance	0.7 mH
Stator resistance	50 mΩ
Delta connected filter capacitors	25 μF each
Switching frequency	10 kHz

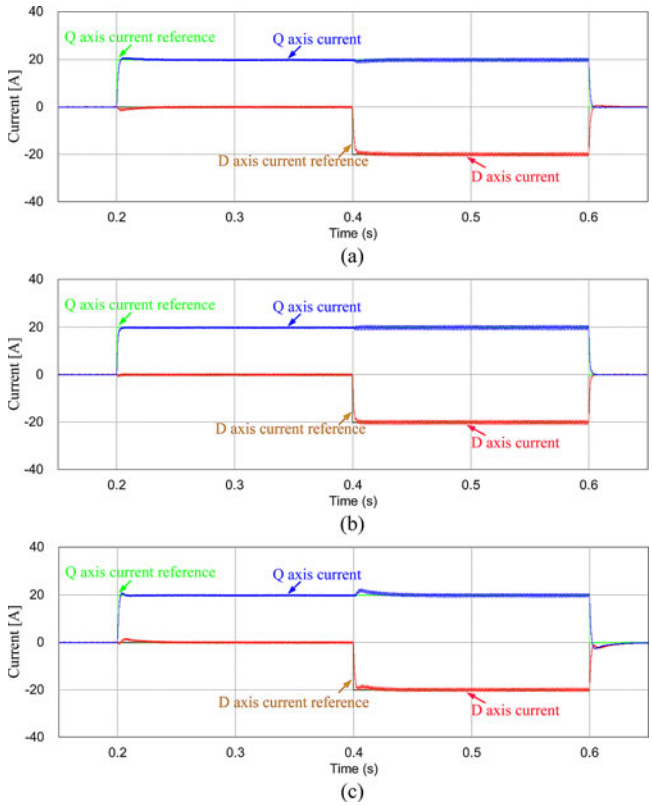

Fig. 25. Simulation result of step response for the feed forward decoupling method. (a) Without the active damping method. (b) With the series active damping method ($R_v = 1\,\Omega$). (c) With the parallel active damping method ($R_p = 20\,\Omega$).

Fig. 25 shows the simulation result of step response of designed controller with the feed forward decoupling method. As shown in Fig. 25(a), without the active damping method, the system is stable. However, it shows undesirable regulation performance as expected from Fig. 14. With the series active damping method which is shown in Fig. 25(b), the system is stable and it shows better regulation performance as expected from Fig. 16. While Fig. 25(c) shows that the system is stable but it has oscillating responses with the parallel active damping method as expected from Fig. 18.

On the other hands, Fig. 26 shows the simulation result of step response of designed controller with the complex vector decoupling method. As shown in Fig. 26(a) and expected from Fig. 15, without the active damping method, the system has poor stability and highly oscillating response. However, with the series active damping method which is shown in Fig. 26(b), as expected from Fig. 17, the system is quite stable and it reveals better regulation performance. Fig. 26(c) shows that the system still has degraded stability and highly oscillating responses with the parallel active damping method as expected from Fig. 19. Thus, the analysis in Section IV has been verified from the simulation results.

In order to verify the designed bandwidth, the settling time was measured by the computer simulation. The settling time is determined by the natural frequency, and it can be calculated by (51). In the simulation, the series active damping method

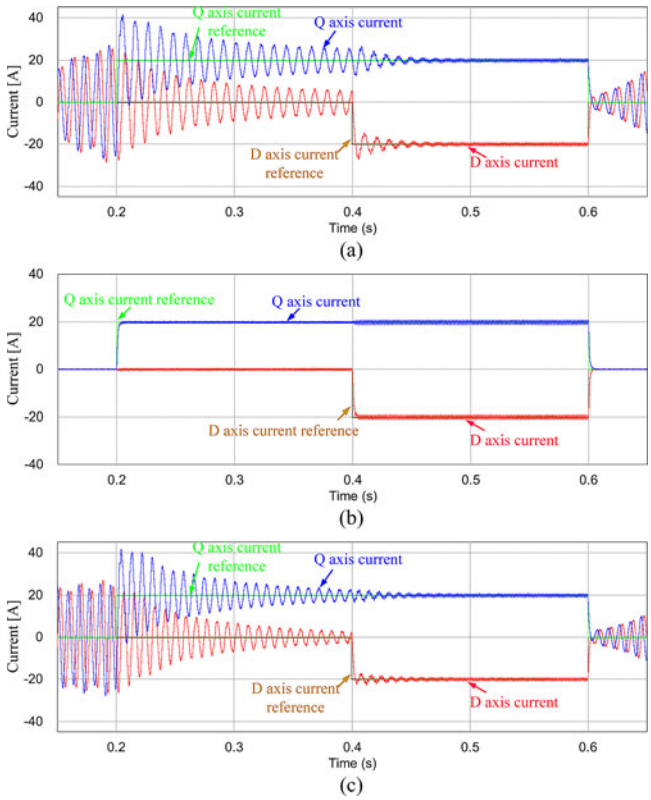

Fig. 26. Simulation result of step response for the complex vector decoupling method. (a) Without the active damping method. (b) With the series active damping method ($R_v = 1\,\Omega$). (c) With the parallel active damping method ($R_p = 20\,\Omega$).

TABLE II
SETTLING TIME OF THE PROPOSED CONTROLLER

Natural frequency	Feed forward decoupling method	Complex vector decoupling method	Calculated settling time by (51)
100 Hz	9.9 ms	9.6 ms	9.3 ms
200 Hz	5.1 ms	5 ms	4.7 ms
300 Hz	3.4 ms	3.3 ms	3.1 ms
400 Hz	2.3 ms	2.5 ms	2.3 ms
500 Hz	2 ms	2 ms	1.9 ms

$R_v = 1\ \Omega$ was used for two proposed decoupling methods. The settling time with the proposed current controller is listed in Table II.

As shown in Table II, the measured settling time is almost the same with the calculated settling time. Thus, the proposed current controller with the series active damping method can satisfy the desired regulation performance despite the error between the continuous model and the discrete model of the multiloop control structure. And also, it can be noted that the proposed method can be used for the general applications because it has a flexibility to select the dynamic performance, which can be determined with the natural frequency.

VI. EXPERIMENTAL RESULTS

Fig. 27 shows the fabricated prototype CSI for a laboratory experiment. The 1200-V–75-A IGBTs and diodes have been used for the prototype CSI. As shown in Fig. 28, an induction machine and a three-phase grid have been used as a load machine for the speed control and the source for the dc-link current control, respectively. An SMPMSM, which has the same nominal parameters with the SMPMSM used in the simulation and its parameters are listed in Table I, has been used as the drive system under the test.

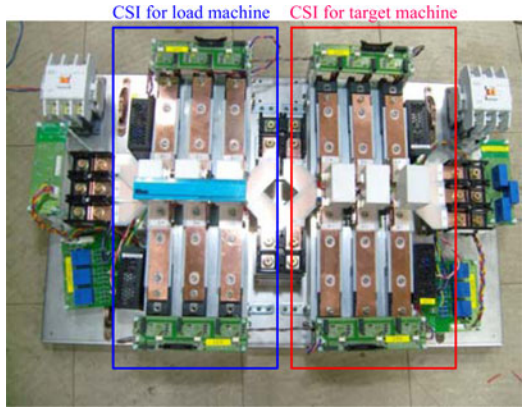

Fig. 27. Prototype CSI for the experiments.

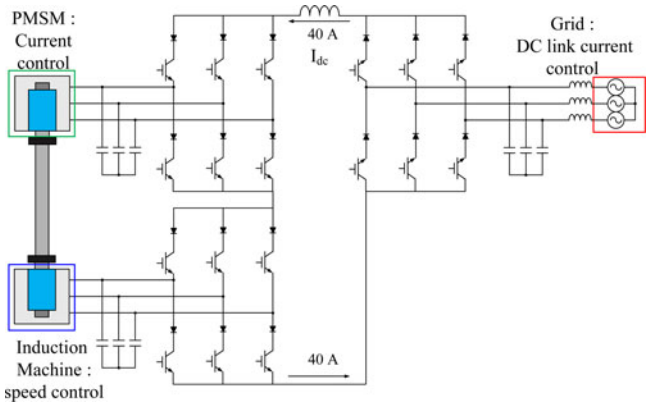

Fig. 28. System configuration for the experiment.

TABLE III
PARAMETERS OF THE INDUCTION MACHINE

Parameter	Value
Rated Power	11 kW
Rated Speed	1750 r/min
Number of Poles	4
Stator resistance	69 mΩ
Rotor resistance	50 mΩ
Stator self inductance	14.1 mH
Rotor self inductance	14.1 mH
Mutual inductance	13.2 mH
Delta connected filter capacitor	25 μF

The parameters of the induction machine are listed in Table III.

In the experiment, the mechanical angular speed of rotor is set to −1000 r/min, which is equivalent to −66.7 Hz in the electric angular frequency and the dc-link current is set to 40-A constant. In addition, the designed transfer function is the same with the simulation as (52).

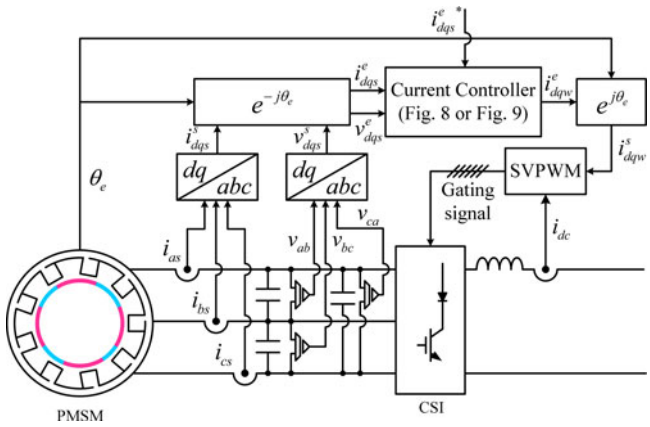

Fig. 29. Control block diagram for the experiment.

Fig. 29 shows the control block diagram for the experiment. The d- and q-axes current in the stationary reference frame are calculated from a, b, and c phase measured current. In addition, the d- and q-axes voltage in the stationary reference frame are calculated from the line-to-line voltage of the delta connected capacitor. The d- and q-axes current and voltage in the synchronous reference frame are calculated using the angle information which can be measured by an encoder signal. To generate the gating signals, the space vector pulsewidth modulation for CSI was adopted [21].

Fig. 30 shows the experimental result of step response of designed controller with the feed forward decoupling method. As shown in Fig. 30(a), without the active damping method, the system is stable. However, it shows undesirable regulation performance as expected from Fig. 14. With the series active damping method which is shown in Fig. 30(b), it shows better regulation performance as expected from Fig. 16, whereas Fig. 30(c) shows that the system is stable but it still shows undesirable responses with the parallel active damping method as expected from Fig. 18.

Fig. 31 shows the experimental result of step response of designed controller with the complex vector decoupling method. As shown in Fig. 31(a) and expected from Fig. 15, without the active damping method, the system has highly oscillating response. However, with the series active damping method which is shown in Fig. 31(b), as expected from Fig. 17, the system is quite stable and it reveals better regulation performance. Fig. 31(c) shows that the system still has oscillating responses and poor regulation performance with the parallel active damping method as expected from Fig. 19.

As mentioned before, the design approach of multiloop controller based on the continuous system has inherent stability issues because of the difference between the continuous model and the discrete model of the cascaded system. And it might incur the instability or degraded dynamic response. However, from the experimental results, the proposed multiloop current controller through the design methodology in the discrete-time domain shows the significantly improved stability and dynamic response using series active damping method.

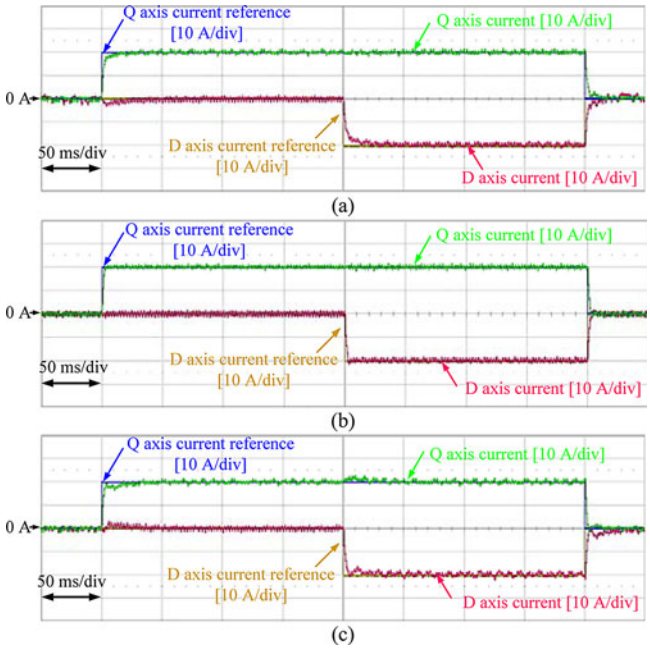

Fig. 30. Experimental result of step response with the feed forward decoupling method. (a) Without the active damping method. (b) With the series active damping method ($R_v = 1\,\Omega$). (c) With the parallel active damping method ($R_p = 20\,\Omega$).

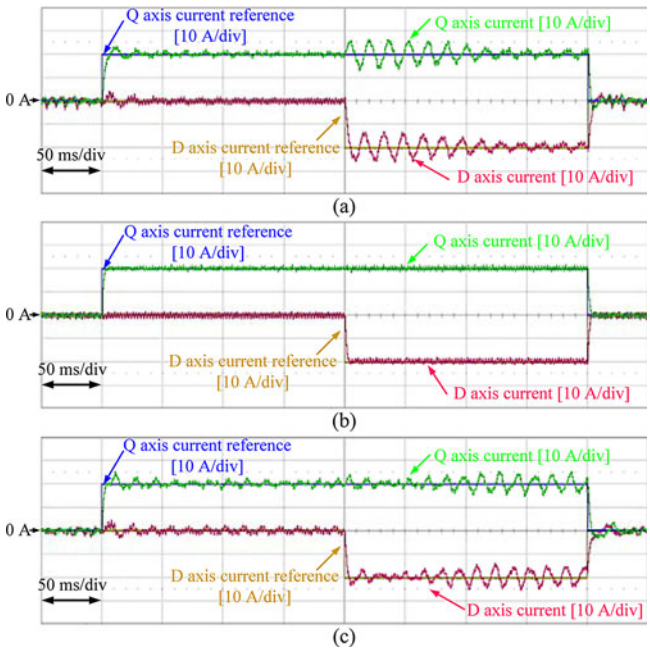

Fig. 31. Experimental result of step response with the complex vector decoupling method. (a) Without the active damping method. (b) With the series active damping method ($R_v = 1\,\Omega$). (c) With the parallel active damping method ($R_p = 20\,\Omega$).

The proposed multiloop controller is designed to have critically damped responses which reveal the fastest response without overshoot. The experimental results represent that the decoupling methods with the series active damping method have the designed settling time of about 3 ms without the overshoot and the coupling effect. It can be noted that the proposed method

TABLE IV
PERFORMANCE OF THE PROPOSED CURRENT CONTROLLER

	Damping method	Stability	Designed settling time	Steady state error	Burden of computation
Feed forward decoupling method	No	Moderate	No	No	Moderate
	Parallel active damping	Moderate	No	No	High
	Series active damping	High	Yes	No	Moderate
Complex vector decoupling method	No	Low	No	No	Low
	Parallel active damping	Low	No	No	Moderate
	Series active damping	High	Yes	No	Low

exhibits reasonable performance as designed. Hence, it is viable to be applied to general drive systems.

VII. SUMMARY

With the simulation and experimental results, Table IV summarizes the performance of each implementation based on the stability, the settling time, a steady-state error and a burden of computation.

The stability of the each method is verified by Section III-B to III-E. And with the series active damping method, each decoupling method can meet the designed settling time which is verified in Table II. There is no steady-state error in each decoupling method because of the integrator which has infinite gain at dc. The burden of computation is mentioned in Section II. In the case of the feed forward decoupling method, the differentiation for the measured current should be applied for the feed forwarding term which can be calculated using the measured voltage and current with the parameters of the ac machine. And to implement the parallel active damping method, the additional integrator and additional feed forwarding term are required in voltage control loop whereas the series active damping method can be implemented with adding the feed forwarding term and simple modification of the integrator gain. Thus, the feed forward decoupling method has higher burden of computation than the complex vector decoupling method and the parallel active damping method needs more computation than the series active damping method does.

VIII. CONCLUSION

In this paper, the multiloop current controller has been proposed for the CSI-fed ac machine drive to avoid the resonance caused by the *LC* filter through the step response. In order to design the multiloop current controller, two-stage modeling has been employed. Additionally, two decoupling methods, namely the feed forward decoupling method and the complex vector decoupling method, have been proposed to decouple the coupling term incurred by the coordinate transformation to the synchronous reference frame. The proposed control scheme is simple and it can be easily implemented. However, the proposed control scheme might have instability or degraded dynamic response due to the intrinsic error between the continuous model and the discrete model of the cascaded control structure due to the *LC* filter. A design methodology considering the digital implementation of the current controller has been described. And, a current controller for the CSI-fed ac machine drive systems has been proposed. In order to avoid instability or degraded dynamic response, the active damping methods based on the virtual resistance has been embedded in the proposed controller. The stability and characteristics of the two decoupling methods have been analyzed in the discrete-time domain using ZOH equivalence. Among the proposed damping methods, the series active damping method has more effectiveness for improved stability and dynamic response than the parallel active damping method in the proposed control scheme has. To validate the effectiveness of the proposed control scheme, simulation, and experimental results have been shown and discussed. The proposed design methodology can be equally applied to not only ac machine drive system, but also other ac systems which have cascaded control structure by simple modification of gains and feed forwarding terms.

REFERENCES

[1] M. Salo and H. Tuusa, "Vector-controlled PWM current-source-inverter-fed induction motor drive with a new stator current control method," *IEEE Trans. Ind. Electron.*, vol. 52, no. 2, pp. 523–531, Apr. 2005.
[2] Z. Wang, B. Wu, D. Xu, and N. R. Zargari, "Hybrid PWM for high-power current-source-inverter-fed drives with low switching frequency," *IEEE Trans. Power Electron.*, vol. 26, no. 6, pp. 1754–1764, Jun. 2011.
[3] J. Dao, D. Xu, and B. Wu, "A novel control scheme for current-source-converter-based PMSG wind energy conversion systems," *IEEE Trans. Power Electron.*, vol. 24, no. 4, pp. 963–972, Apr. 2009.
[4] J. Dao, D. Xu, B. Wu, and N. R. Zargari, "Unified DC-link current control for low-voltage ride-through in current-source-based wind energy conversion systems," *IEEE Trans. Power Electron.*, vol. 26, no. 1, pp. 288–297, Jan. 2011.
[5] Z. Wu and G. J. Su, "High-performance permanent magnet machine drive for electric vehicle applications using a current source inverter," in *Proc. Conf. IEEE Ind. Electron.*, Nov. 2008, pp. 2812–2817.
[6] H. Bilgin and M. Ermis, "Design and implementation of a current-source converter for use in industry applications of D-STATCOM," *IEEE Trans. Power Electron.*, vol. 25, no. 8, pp. 1943–1957, Aug. 2010.
[7] J. C. Wiseman and B. Wu, "Active damping control of a high-power PWM current-source rectifier for line-current THD reduction," *IEEE Trans. Ind. Electron.*, vol. 52, no. 3, pp. 758–764, Jun. 2005.
[8] F. Liu, B. Wu, N. R. Zargari, and M. Pande, "An active damping method using inductor-current feedback control for high-power PWM current-source rectifier," *IEEE Trans. Power Electron.*, vol. 26, no. 9, pp. 2580–2587, Sep. 2011.
[9] M. Salo and H. Tuusa, "A vector controlled current-source PWM rectifier with a novel current damping method," *IEEE Trans. Power Electron.*, vol. 15, no. 3, pp. 464–470, May 2000.
[10] Y. Neba, "A simple method for suppression of resonance oscillation in PWM current source converter," *IEEE Trans. Power Electron.*, vol. 20, no. 1, pp. 132–139, Jan. 2005.
[11] Y. W. Li, B. Wu, N. R. Zargari, J. C. Wiseman, and D. Xu, "Damping of PWM current-source rectifier using a hybrid combination approach," *IEEE Trans. Power Electron.*, vol. 22, no. 4, pp. 132–139, Jul. 2007.
[12] P. C. Loh and D. G. Holmes, "Analysis of multiloop control strategies for LC/CL/LCL-filtered voltage-source and current-source inverters," *IEEE Trans. Ind. Appl.*, vol. 41, no. 2, pp. 644–654, Mar./Apr. 2005.
[13] Y. W. Li, "Control and resonance damping of voltage-source and current-source converters with *LC* filters," *IEEE Trans. Ind. Electron.*, vol. 56, no. 5, pp. 1511–1521, May 2009.
[14] F. Briz, M. W. Degner, and R. D. Lorenz, "Analysis and design of current regulators using complex vectors," *IEEE Trans. Ind. Appl.*, vol. 36, no. 3, pp. 817–825, May/Jun. 2000.

[15] D. M. Van de Sype, K. D. Gusseme, F. M. L. L. De Beliem, A. P. Van den Bossche, and J. A. Melkebeek, "Small-signal z-domain analysis of digitally controlled converters," *IEEE Trans. Power Electron.*, vol. 21, no. 2, pp. 470–478, Mar. 2006.
[16] H. Kim, M. W. Degner, J. M. Guerrero, F. Briz, and R. D. Lorenz, "Discrete-time current regulator design for AC machine drives," *IEEE Trans. Ind. Appl.*, vol. 46, no. 4, pp. 1425–1435, Jul./Aug. 2010.
[17] B. P. McGrath, S. G. Parker, and D. G. Holmes, "High performance current regulation for low pulse ratio inverters," in *Proc. IEEE Energy Convers. Congr. Expo.*, Sep., 2011, pp. 750–757.
[18] K. Ogata, *Discrete-Time Control Systems*, 2nd ed. Englewood Cliffs, NJ: Prentice Hall, 1995.
[19] J. Holtz, J. Quan, J. Pontt, J. Rodriguez, P. Newman, and H. Miranda, "Design of fast and robust current regulators for high-power drives based on complex state variables," *IEEE Trans. Ind. Appl.*, vol. 40, no. 1, pp. 1388–1397, Sep./Oct. 2004.
[20] B. H. Bae and S. K. Sul, "A compensation method for time delay of full-digital synchronous frame current regulator of PWM AC drives," *IEEE Trans. Ind. Appl.*, vol. 39, no. 3, pp. 802–810, May/Jun. 2003.
[21] Y. W. Li, B. Wu, D. Xu, and N. R. Zargari, "Space vector sequence investigation and synchronization methods for active front-end rectifiers in high-power current-source drives," *IEEE Trans. Ind. Electron.*, vol. 55, no. 3, pp. 1022–1034, Mar. 2008.

Hak-Jun Lee (S'11) was born in Korea in 1980. He received the B.S. and M.S. degrees in electrical engineering from Seoul National University, Seoul, Korea, in 2007 and 2009, respectively, where he has been working toward the Ph.D. degree.

His current research interests include high-power converter, multilevel converter, and electric/hybrid vehicle drives.

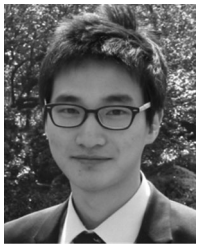

Sungho Jung (S'11) was born in Busan, Korea, in 1984. He received the B.S. degree in electronic and electrical engineering from Pusan National University, Busan, Korea, in 2010, and the M.S. degree in electrical engineering and computer science from Seoul National University, Seoul, Korea, in 2012, where he is currently working toward the Ph.D. degree in electrical engineering and computer science.

His current research interests are power conversion system and electric machine drives.

Seung-Ki Sul (S'78–M'80–SM'98–F'00) was born in Korea in 1958. He received the B.S., M.S., and Ph.D. degrees in electrical engineering from Seoul National University, Seoul, Korea, in 1980, 1983, and 1986, respectively.

From 1986 to 1988, he was an Associate Researcher with the Department of Electrical and Computer Engineering, University of Wisconsin, Madison. From 1988 to 1990, he was a Principal Research Engineer with Gold-Star Industrial Systems Company. Since 1991, he has been a Professor of the School of Electrical Engineering and Computer Science, Seoul National University, where he was the Vice Dean from 2005 to 2007, and was the President of the Korea Electrical Engineering and Science Research Institute from 2008 to 2011. His current research interests include power-electronic control of electric machines, electric/hybrid vehicle drives, and power-converter circuits.